

# Adaptively Reforming Natural Enzyme to Activate Catalytic Microenvironment for Polysulfide Conversion in Lithium–Sulfur Batteries

Ce Liang, Shuo Yang,\* Dong Cai,\* Jun Liu, Shuang Yu, Tingting Li, Haohao Wang, Yahui Liu, Huagui Nie,\* and Zhi Yang\*



Cite This: <https://doi.org/10.1021/acsami.2c18976>



Read Online

ACCESS |



Metrics & More



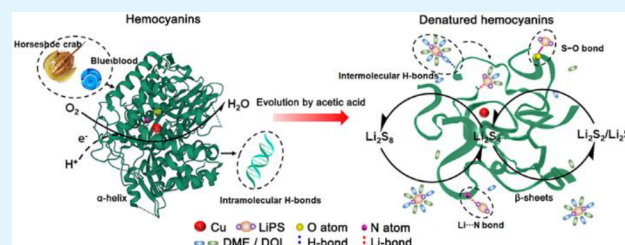
Article Recommendations



Supporting Information

**ABSTRACT:** Catalyzing polysulfide conversion is a promising way toward accelerating complex and sluggish sulfur redox reactions (SRRs) in lithium–sulfur batteries. Reasonable alteration of an enzyme provides a new means to expand the natural enzyme universe to catalytic reactions in abiotic systems. Herein, we design and fabricate a denatured hemocyanin (DHc) to efficiently catalyze the SRR. After denaturation, the unfolded  $\beta$ -sheet architectures with exposed rich atomically dispersed Cu, O, and N sites and intermolecular H-bonds are formed in DHc, which not only provides the polysulfides for a strong spatial confinement effect in microenvironment via S–O and Li $\cdots$ N interactions but also activates chemical channels for electron/Li<sup>+</sup> transport into the Cu active center via H/Li-bonds to catalyze polysulfide conversion. As expected, the charge/discharge kinetics of DHc-containing cathodes is fundamentally improved in cyclability with nearly 100% Coulombic efficiency and capacity even under high sulfur loading (4.3 mg cm<sup>-2</sup>) and lean-electrolyte (8  $\mu$ L mg<sup>-1</sup>) conditions.

**KEYWORDS:** lithium–sulfur battery, polysulfide conversion, hemocyanin, denaturation, catalytic microenvironment



## 1. INTRODUCTION

Advanced energy storage devices with a high energy density exceeding that of lithium-ion batteries are highly desirable for the continuing development of electric vehicles and portable electronics. Among various developed battery candidates, lithium–sulfur (Li–S) batteries employing eco-friendly and cost-effective sulfur as a cathode are becoming increasingly sought after due to their high theoretical energy density (2600 Wh kg<sup>-1</sup>).<sup>1,2</sup> Despite their promising prospects, the severe shuttling of lithium polysulfides (LiPSs) between the sulfur cathode and lithium anode accompanied by slow reaction kinetics gives rise to the loss of active sulfur, rapid capacity fading, and low Coulombic efficiency, which markedly handicaps the practical application of Li–S batteries.

In the past decades, tremendous efforts have been made to overcome these issues through developing catalyst materials decorated on a sulfur cathode or separator in a Li–S realm.<sup>3–5</sup> In this regard, various solid catalysts encompassing metal,<sup>6,7</sup> metal compounds,<sup>8,9</sup> and their heterostructures,<sup>10</sup> have been introduced to promote the sulfur conversion reaction, block LiPS migration, and improve the kinetic properties of the batteries. Despite their favorable regulation over the adsorption–catalysis–conversion of LiPSs to a certain extent, the electrochemical performances of the batteries remain unsatisfactory, especially under the conditions of high sulfur loading and lean electrolyte, mainly due to the complexity of

the sulfur redox reaction (SRR) mechanism involving a sequence of dynamically changing liquid and solid equilibria and the incompatibility of highly catalytic activity and excellent stability for the existing solid catalysts. Thereby, further suitable catalyst alternatives should be developed for an efficient and stable Li–S battery technology.

The solution to a complex science problem is often to use complex system design. Enzymes have been subject to millions of years of evolutionary experimentation, giving rise to very intricate and delicate structures. As nature's privileged catalysts, enzymes are well-known for their amazing ability to exert exquisite control over the stereochemical outcome of chemical reactions.<sup>11</sup> Native hemocyanins (Hcs) with enzymatic activity are often found in many deep-sea organisms that have evolved for a billion years.<sup>12</sup> As an oxygen carrier protein, Hc can reversibly bind with oxygen by its centered Cu atom pair and has exhibited good catalytic activity for the oxygen reduction reaction (ORR) in our previous study (Figure S1). Recently proposed periodic expansion catalysis<sup>13</sup>

**Received:** October 21, 2022

**Accepted:** December 16, 2022

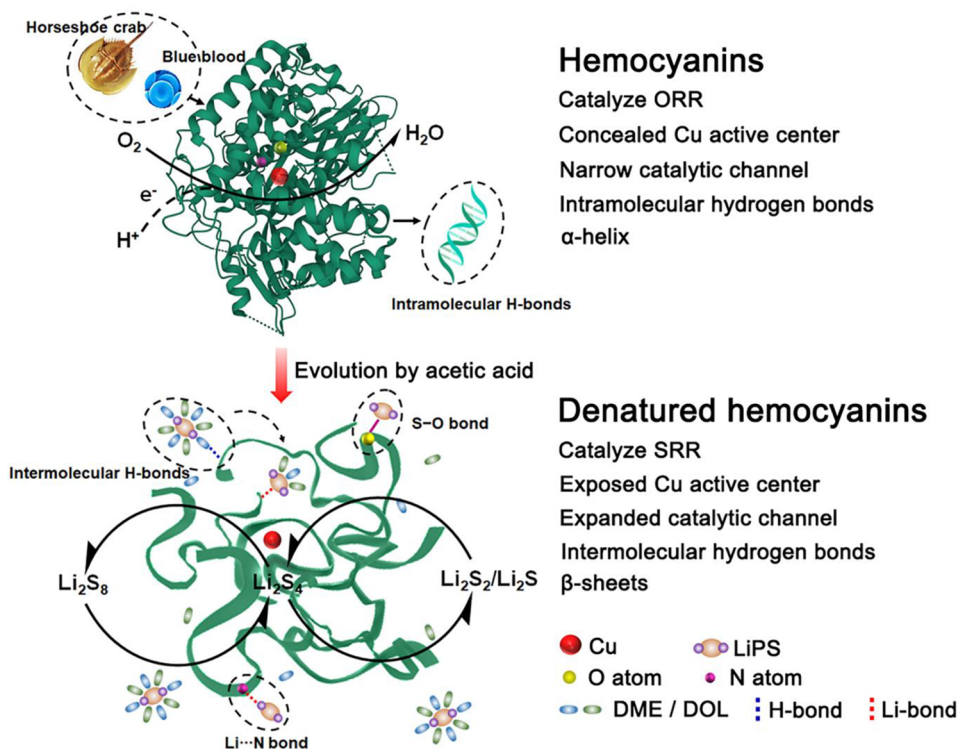


**Figure 1.** Schematic illustration of the inspiration for DHc design from biochemistry to Li-S chemistry.

motivates us to relate the ORR activity of Hc to its potential in catalyzing the SRR, since S and Li elements are located in the next period of O and H in the periodic table of elements. From a physicochemical perspective, Hc with hierarchical structures should be a potential catalyst candidate due to its active Cu center allowing electrochemical catalysis of trapped LiPSs and an enormous number of O and N atoms on the protein backbones, providing rich and atomically dispersed binding sites to LiPSs. Nonetheless, different from the aqueous media for conventional enzymatic catalysis in living species, the organic solvents of the Li-S system may cause poor electrochemical stabilities and unsatisfactory catalytic activities of Hcs. Moreover, a growing consensus is that enzymatic catalysis depends not only on the active center but also on the microenvironment surrounding the active center. When the confined nanospace in the microenvironment is close to the guest molecular size, a fascinating reactant activation and transformation can take place there. In Hcs, the long-branched chains and folded structure severely block the access of active sites in the protein for trapping and catalyzing LiPSs. Thus, the direct application of Hc for SRR catalysis seems inadvisable. Over the past decades, the advent of directed evolution has enabled the rapid development of customized enzymes to generate excellent activity and stereoselectivity for nonconventional environments.<sup>14,15</sup> Inspired by this, we were motivated to adaptively reform Hcs to address the challenge in interacting with LiPSs in Li-S batteries.

In the current work, we designed and fabricated denatured hemocyanins (DHcs) through a precise acidification treatment to form an effective catalyst for a fast-converting LiPS cathode. A comprehensive investigation of the structure and mechanism of DHcs reveals that, thanks to the unfolded  $\beta$ -sheet structure, fully exposed Cu, O, and N sites, and expanded catalytic channels, the solvated LiPS clusters can be efficiently

concentrated in the microenvironment of DHcs through the formation of intermolecular H-bonds with large amounts of exposed functional groups on the protein skeleton, and then the desolvated LiPS interacts with the functional groups via S-O bonds and Li-bonds, accelerating electron/Li<sup>+</sup> transport into the center Cu active site and facilitating LiPS conversion (Figure 1). Through the synergistic effect of the LiPS enrichment effect on the reaction microenvironment and reduced steric hindrance for catalytically active sites, significant improvements in the electrochemical performance of Li-S batteries are achieved by introducing DHcs. This work presents that employing a customized enzyme to confine LiPSs in a microenvironment is a promising approach to achieve an efficient catalytic system for sulfur conversion, structure identification, and catalysis understanding.

## 2. RESULTS AND DISCUSSION

Figure 1 illustrates the process of DHcs obtained by adaptive reform of natural Hc, where the reformed environment is carefully optimized by adjusting the concentration of acetic acid solution and soaking time (Figure S2). It can be clearly seen that, with the strong interchain interactions (e.g., hydrogen bonds, disulfide bonds, and salt bridges), the major molecular conformation of the Hcs either randomly coils or folds into different shapes, which conceals the Cu active center and a large amount of functional groups inside the protein chains,<sup>16</sup> probably weakening the functional activities of Hcs for the SRR. The denaturation treatment of the Hc can break down its secondary and even higher levels of protein structures,<sup>17</sup> which is necessary to expand the chains and expose the Cu active center and polar/nonpolar functional groups that are hidden in the native protein for interacting with other components outside. The detailed structural transition and physicochemical property change of the DHcs were

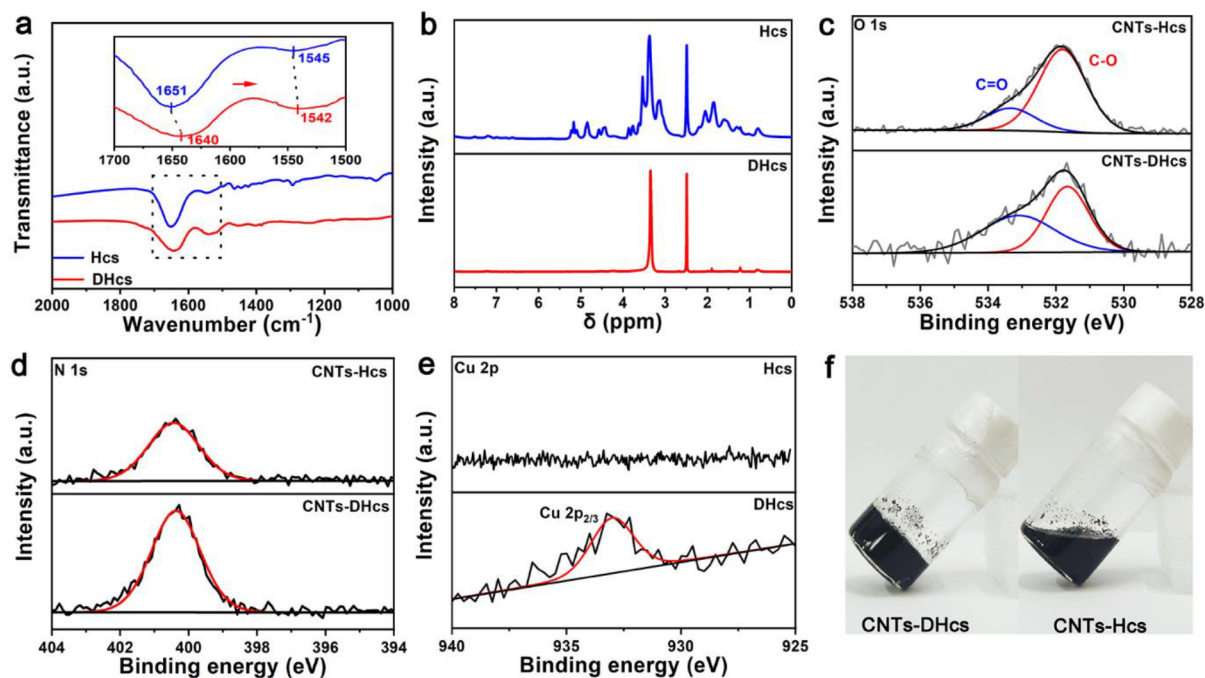


**Figure 2.** (a) FTIR spectra of Hcs and DHcs. (b)  $^1\text{H}$  NMR spectra of Hcs and DHcs. (c–e) High-resolution XPS spectra of (c) O 1s, (d) N 1s, and (e) Cu 2p peaks for Hcs and DHcs. (f) Digital photos of CNTs-Hcs and CNTs-DHcs slurries in tilted bottles, showing the different viscosities of the samples.

carefully verified on both microcosmic and macroscopic scales. From a microcosmic perspective, Fourier-transformed infrared (FTIR) spectroscopy was first applied to measure the secondary structural transformation of DHcs. As shown in Figure 2a, the broad peak located at  $1651\text{ cm}^{-1}$  of the pristine Hcs associated with the amide I band from a C=O stretching vibration with minor contribution from N–H in-plane bending<sup>18</sup> significantly shifts to  $1640\text{ cm}^{-1}$  after denaturation, while the original peak at around  $1545\text{ cm}^{-1}$  corresponding to amide II from C–N stretching and N–H in-plane bending<sup>10</sup> moves to  $1542\text{ cm}^{-1}$ . The shifts of the signature FTIR peaks unambiguously indicate that the secondary structures of Hc molecules transform from the original  $\alpha$ -helix to  $\beta$ -sheets after denaturation.<sup>19</sup> To further confirm such a secondary structural transformation, a hydrogen bond as an important part of a secondary structure is necessary to be checked by  $^1\text{H}$  NMR. As shown in Figure 2b, most resonance signals are lost at DHcs, which could be a consequence of hydrogen bond breaking and opening of Hc proteins, where the intramolecular H-bonds might transform to intermolecular H-bonds.<sup>20</sup> The intermolecular H-bonds could be beneficial to form H-bonds with the solvated LiPS clusters in the electrolyte (Figure 1). X-ray diffraction (XRD) patterns in Figure S3 show that the denaturation process reduces the crystallinity of Hcs due to the unfolding effect. To further understand how the denaturants affect the unfolded structure, X-ray photoelectron spectroscopy (XPS) measurements were performed, and the results are illustrated in Figure 2c–e. Compared with the CNTs-Hcs, the increased C=O ( $533.3\text{ eV}$  in Figure 2c)<sup>21</sup> and N–H ( $400.4\text{ eV}$  in Figure 2d)<sup>22</sup> intensities in CNTs-DHcs indicate an unwinding of peptide chains by breaking amide bonds and more O- and N-containing functional groups are exposed in DHcs after the unfolding process. The detectable Cu signal in the Cu 2p XPS spectrum of DHcs (Figure 2e)

further prove that the curled structure of Hc is open and Cu active centers are exposed after the denaturation process.

These structural changes in the enzyme induced by denaturation can also be reflected at the macroscopic scale. It is well-known that enzymes with a higher degree of denaturation show greater viscosities because of the more expansive and disentangled protein coils.<sup>23</sup> As clearly shown in Figure 2f, the CNTs-DHcs slurry exhibits lower liquidity and greater viscosity than the CNTs-Hcs slurry when the bottles are tilted, implying the DHcs have a stronger intermolecular H-bonding and a more expanded molecular configuration due to a lower folding degree. The two slurries without addition of polyvinylidene fluoride (PVDF) binder were further coated on Al foils with a blade, respectively. The significant differences can be clearly observed by digital photos (Figure S4) and SEM images (Figure S5), in which the CNTs-DHcs film presents smoother and more uniform surface than the CNTs-Hcs film. In addition, the as-fabricated CNTs-DHcs film displays good mechanical durability under extreme conditions (Figure S6). These results demonstrate that, with the fully exposed O- and N-containing functional groups, the CNTs-DHcs film becomes more compact and can exert stronger adhesion to the Al foil, again confirming the changes in denaturation or unfolding degree of Hc molecules. Since the wettability between the electrode and the electrolyte interface is an important factor to determine the electrochemical performances, we measured the contact angles of the electrolyte on different electrode surfaces. As shown in Figure S7, the static contact angle of an electrolyte droplet on the CNTs-DHcs surface ( $8^\circ$ ) is smaller than that on CNTs-Hcs ( $12^\circ$ ) and CNTs ( $15^\circ$ ), revealing its better penetration of electrolyte, where more exposed functional groups in DHcs may have favorable chemical interactions with the electrolyte solvent molecules. The improved electrode wettability by DHcs is beneficial to promote the redox reaction of the dissolved LiPSs in the electrolyte, improve the utilization

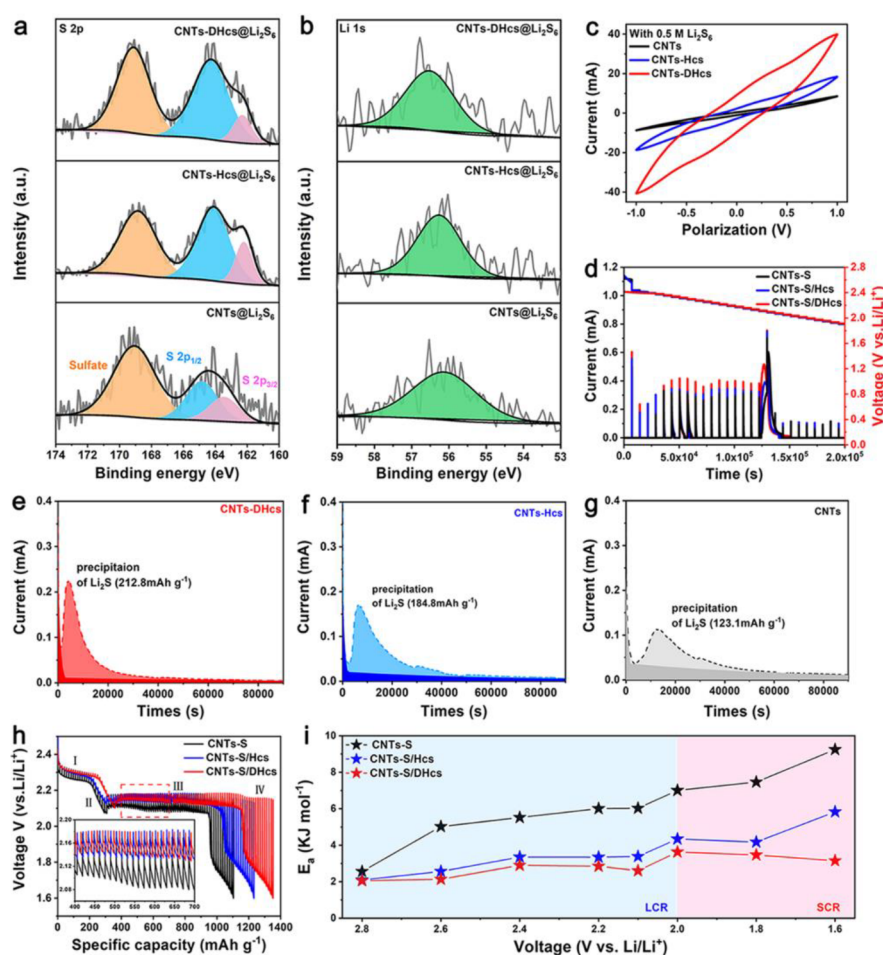


**Figure 3.** (a, b) High-resolution (a) S 2p and (b) Li 1s XPS spectra of CNTs-DHcs, CNTs-Hcs, and CNTs after Li<sub>2</sub>S<sub>6</sub> adsorption. (c) Cyclic voltammetry profiles in Li<sub>2</sub>S<sub>6</sub> symmetrical cells based on CNTs-DHcs, CNTs-Hcs, and CNTs electrodes at 10 mV s<sup>-1</sup>. (d) PITT plots of the cells with CNTs-S/DHcs, CNTs-S/Hcs, and CNTs-S cathodes under a discharge operation from 2.6 to 1.6 V with a step of 0.02 V. (e–g) Potentiostatic discharge profiles of (e) CNTs-DHcs, (f) CNTs-Hcs, and (g) CNTs in Li<sub>2</sub>S<sub>6</sub> solution at 2.05 V on CNTs-DHcs, CNTs-Hcs, and CNTs electrodes. (h) GITT profiles of the cells with CNTs-S/DHcs, CNTs-S/Hcs, and CNTs-S cathodes during the second discharge at 0.05 C. (i) Activation energy profiles of the three electrodes during discharge (LCR, long-chain LiPS conversion reaction; SCR, short-chain LiPS conversion reaction).

of sulfur, and suppress the shuttle effect to afford a highly robust Li–S battery.

The catalytic process of LiPSs includes two critical steps: i.e., adsorption and conversion.<sup>24–26</sup> The static LiPS adsorption experiments (Figure S8) convincingly demonstrate that DHcs have stronger adsorptivity toward LiPSs and substantial remediation of LiPS shuttling, which can be correlated to more available adsorbing sites on DHcs. To reveal the possible interaction mechanism between LiPSs and DHcs, XPS analyses were further performed using the spent samples after visual adsorption. The high-resolution XPS spectrum of S 2p in Figure 3a shows that compared with those for CNTs-Hcs@Li<sub>2</sub>S<sub>6</sub> and CNTs@Li<sub>2</sub>S<sub>6</sub>, the polysulfide peaks for CNTs-DHcs@Li<sub>2</sub>S<sub>6</sub> greatly increase in intensity and shift to lower binding energy, suggesting more LiPS adsorption on DHcs and a stronger electron transfer from DHcs to LiPSs. Meanwhile, there is a shift to higher binding energy in the O 1s XPS spectrum of CNTs-DHcs@Li<sub>2</sub>S<sub>6</sub> (Figure S9), further implying more O sites in DHcs fully bond with the S atoms in Li<sub>2</sub>S<sub>6</sub>. Analogously, the Li 1s XPS spectrum of CNTs-DHcs@Li<sub>2</sub>S<sub>6</sub> (Figure 3b) shows a single peak belonging to the Li–S bond at 56.5 eV, which is located at higher binding energy than the Li–S peaks of CNTs-Hcs@Li<sub>2</sub>S<sub>6</sub> and CNTs@Li<sub>2</sub>S<sub>6</sub>, while the

binding energy of its N 1s peak is lower than that of CNTs-Hcs@Li<sub>2</sub>S<sub>6</sub> (Figure S10), demonstrating the formation of a “lithium bond”-like Li⋯N bond<sup>27</sup> that favors a greater electron transfer between LiPSs and DHcs. The above results are indicative of the stronger chemical interaction between sulfur species and DHcs through S–O and Li⋯N bonding. Since the Hc molecule is composed of only one Cu<sup>+</sup> and a peptide chain with more than 200 amino acids, it is difficult to probe the Cu XPS signal from Hc or DHc with the Li<sub>2</sub>S<sub>6</sub> cover in our experiments.

Besides the prerequisite step of static adsorption LiPS behaviors, the promoted catalytic effect of DHcs in LiPS conversion, regarding liquid–liquid conversion and liquid–solid conversion, was also kinetically demonstrated. The liquid–liquid transformation kinetics of long-chain LiPSs to short-chain LiPSs were first characterized by the cyclic voltammetry (CV) profiles in Li<sub>2</sub>S<sub>6</sub> symmetrical cells. With the addition of DHcs, the symmetrical cells exhibit 4-fold and 2-fold enhancements in polarization current in comparison with those of CNTs and CNTs-Hcs electrodes, respectively (Figure 3c), corresponding to a double interfacial reactivity of the polysulfide electrochemistry facilitated by the Cu, O, and N polar sites. A similar conclusion can also be obtained from the

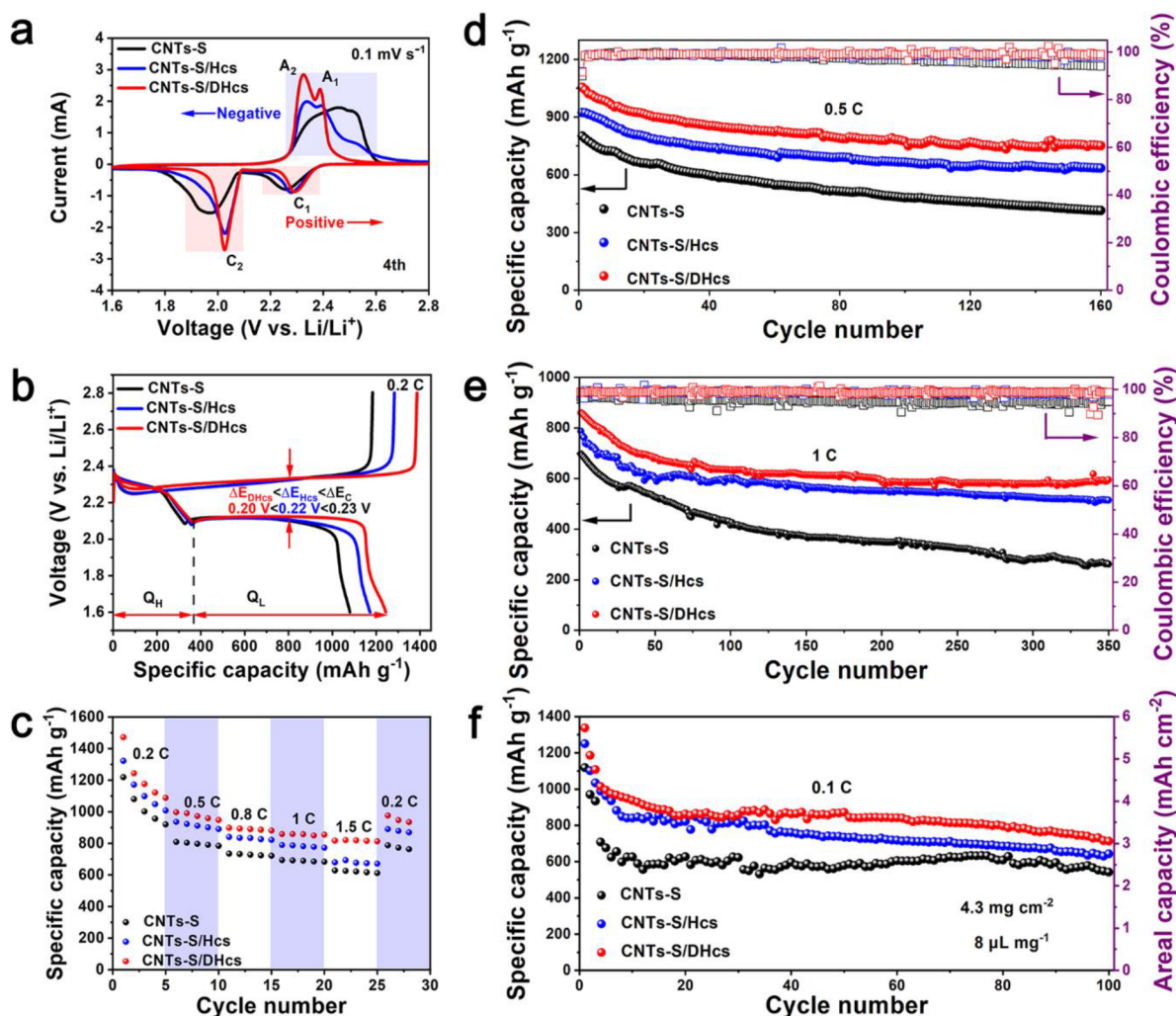


**Figure 4.** (a) Fourth-cycle CV profiles of CNTs-S/DHcs, CNTs-S/Hcs, and CNTs-S cathodes at a scan rate of  $0.1 \text{ mV s}^{-1}$ . (b) Galvanostatic discharge–charge curves of CNTs-S/DHcs, CNTs-S/Hcs, and CNTs-S cathodes at  $0.2 \text{ C}$  for the second cycle.  $\Delta E$  is the voltage gap between the charge and discharge plateaus.  $Q_H$  is the capacity of the upper discharge plateau, and  $Q_L$  is the capacity of the lower discharge plateau. (c) Rate capabilities of different cathodes at varying current densities (from  $0.2$  to  $1.5 \text{ C}$  and back to  $0.2 \text{ C}$ ). (d, e) Cycling performance of CNTs-S/DHcs, CNTs-S/Hcs, and CNTs-S cathodes at (d)  $0.5 \text{ C}$  and (e)  $1 \text{ C}$ . (f) Cycling performance of CNTs-S/DHcs, CNTs-S/Hcs, and CNTs-S cathodes with a high sulfur loading of  $\sim 4.3 \text{ mg cm}^{-2}$  and an E/S ratio of  $8 \mu\text{L mg}^{-1}$  at  $0.1 \text{ C}$ .

potentiostatic intermittent titration technique (PITT) curves (Figure 3d), in which the CNTs-S/DHcs cell manifests the highest potentiostatic current of above  $2.09 \text{ V}$ .

Another core step in the sulfur conversion reaction is the liquid–solid conversion from soluble short-chain LiPSs to solid  $\text{Li}_2\text{S}_2/\text{Li}_2\text{S}$ , which is deemed to be the “rate-determining” step requiring a large energy barrier. As witnessed in PITT profiles at a lower titration potential of  $2.11 \text{ V}$  (Figure 3d) and  $\text{Li}_2\text{S}$  nucleation experiments (Figure 3e–g), the current intensity ( $0.22 \text{ mA}$ ), peak response time ( $4557 \text{ s}$ ), and calculated nucleation capacity ( $212.8 \text{ mAh g}^{-1}$ ) of CNTs-DHcs cell are superior to those of CNTs-Hcs ( $0.17 \text{ mA}$ ,  $6309 \text{ s}$ ,  $184.8 \text{ mAh g}^{-1}$ ) and CNTs ( $0.11 \text{ mA}$ ,  $12870 \text{ s}$ ,  $123.1 \text{ mAh g}^{-1}$ ) cells, indicative of the unwound architectures and more exposed catalytically active sites in DHcs being in favor of expediting  $\text{Li}^+$  transport and liquid–solid conversion kinetics.<sup>28</sup> Furthermore, the galvanostatic intermittent titration technique (GITT) profile of the battery with a CNTs-S/DHcs cathode (Figure 3h) shows faster recovery and a longer second platform during the titration compared with the counterparts,<sup>29</sup> and its  $\text{Li}^+$  diffusion coefficient ( $D_{\text{Li}^+}$ ) at the liquid–

solid conversion stage (Step III) is elevated 40 and 3.3 times, compared to the values for CNTs-S- and CNTs-S/Hcs-based cells, respectively (Figure S11), confirming the best function of DHcs in promoting  $\text{Li}^+$  diffusion and activating the lithiation kinetics, especially from short-chain LiPSs to solid  $\text{Li}_2\text{S}_2/\text{Li}_2\text{S}$ .

Since the sulfur conversion reaction kinetics is fundamentally reflected by the activation energy ( $E_a$ ) at each step, the  $E_a$  value during discharge was determined herein by detecting the charge transfer resistances ( $R_{\text{ct}}$ ) of the cells at different potentials in the range of  $10$ – $40 \text{ }^\circ\text{C}$  and fitting according to the Arrhenius equation (Figures S12–S15).<sup>30</sup> As shown in Figure 3i, the  $E_a$  value of the cell with DHcs shows a value ( $\sim 2.06 \text{ kJ mol}^{-1}$ ) similar to those of the other two cells (CNTs-S/Hcs and CNTs-S) at  $2.8 \text{ V}$  (conversion from  $\text{S}_8$  to  $\text{Li}_2\text{S}_8$ ) but much lower values ( $3.14$ – $3.63 \text{ kJ mol}^{-1}$ ) than for CNTs-S/Hcs and CNTs-S-based cells especially at  $2.0$ – $1.6 \text{ V}$  (conversion of LiPSs to insoluble  $\text{Li}_2\text{S}_2/\text{Li}_2\text{S}$  products), again confirming that DHcs could facilitate the rate-determining step for Li–S batteries, which is expected to increase the capacity and stability of the batteries.

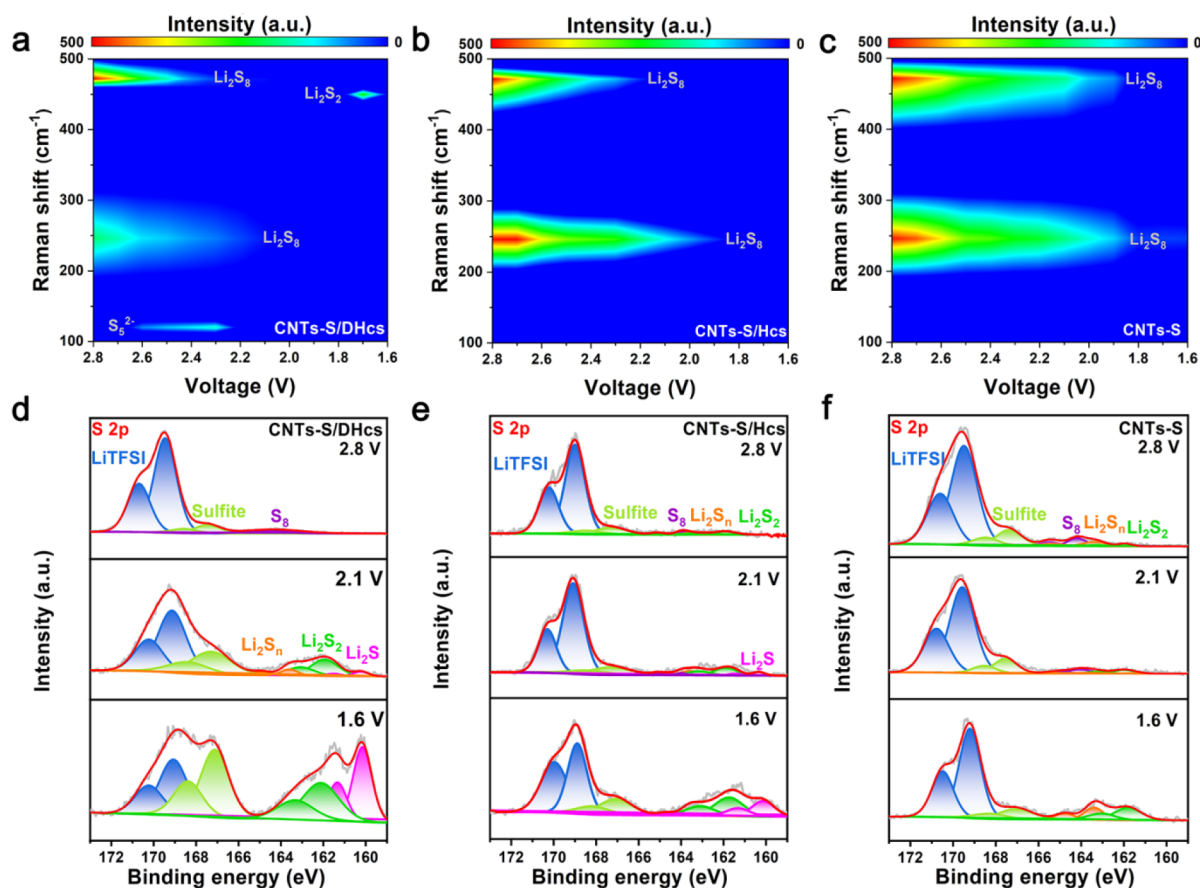


**Figure 5.** (a–c) *In situ* Raman contour mapping images of various sulfur species on (a) CNTs-S/DHcs, (b) CNTs-S/Hcs, and (c) CNTs-S cathodes during the discharging process. (d–f) Quasi *in situ* S 2p XPS spectra of (d) CNTs-S/DHcs, (e) CNTs-S/Hcs, and (f) CNTs-S cathodes during the discharging process.

To comprehensively probe the electrocatalytic effect of Hcs upon enhancing electrochemical performance, CNTs-S/DHcs, CNTs-S/Hcs, and CNTs-S were employed as cathodes in typical Li–S coin-type cells. The CVs of the cells for the first four cycles are depicted in Figure S16. The peak positions and current intensities for CNTs-S/DHcs cathode show no obvious changes after four successive cycles, verifying the highly reversible sulfur conversion process occurring inside of the cell with the CNTs-S/DHcs cathode. The fourth-cycle CV profiles of the three cathodes are further compared in Figure 4a. It can be clearly observed that, in contrast to the redox peaks of the CNTs-S cathode, the two sharper cathodic peaks for CNTs-S/Hcs cathode are positively shifted by ~22 and 48 mV, respectively, whereas its anodic peaks are negatively shifted by ~65 mV. This implies that Hcs can effectively reduce the polarization and accelerate the electrochemical kinetics of sulfur species.<sup>31</sup> Note that the CNTs-S/DHcs cathode displays the smallest polarization (Figure S17) and the largest current intensity especially at C<sub>2</sub> and A<sub>2</sub> as compared to its counterparts, which indicates that the conversion rate between soluble LiPSs and insoluble Li<sub>2</sub>S<sub>2</sub>/Li<sub>2</sub>S and the corresponding capacity values are particularly improved by the superior electrocatalytic activity of DHcs.<sup>32</sup>

To confirm the CV results, Li–S cells with different cathodes were subjected to galvanostatic discharge and charge tests at 0.2 C (1 C = 1675 mAh g<sup>-1</sup>), as shown in Figure 4b. Similar Q<sub>H</sub> values are observed for CNTs-S/DHcs (367.5 mAh g<sup>-1</sup>) and CNTs-S/Hcs (357.4 mAh g<sup>-1</sup>) cathodes, which are

higher than that for CNTs-S, indicating that both DHcs and Hcs can catalyze the liquid–liquid conversion of sulfur. Unlike the case for Q<sub>H</sub>, the CNTs-S/DHcs cathode has a much greater Q<sub>L</sub> (876.6 mAh g<sup>-1</sup>) than CNTs-S/Hcs (814.3 mAh g<sup>-1</sup>) and CNTs-S (753.0 mAh g<sup>-1</sup>). The highest Q<sub>L</sub>/Q<sub>H</sub> and the smallest interfacial energy barrier (0.2 mV) observed for CNTs-S/DHcs provide further evidence regarding the most prominent liquid–solid reaction kinetics on the CNTs-S/DHcs cathode. Equally important, the Q<sub>L</sub>/Q<sub>H</sub> ratio of CNTs-S/DHcs at 1.5 C is almost 1.5 times that of CNTs-S (Figure S18), implying that the use of DHcs greatly extends the life of Li–S batteries at relatively high rates. Apart from that, the CNTs-S/DHcs cell exhibits a smaller voltage hysteresis (ΔE) compared with CNTs-S/Hcs and CNTs-S cells, demonstrating reduced electrochemical polarization benefiting from the catalytic activity of DHcs toward sulfur redox reactions, in agreement with the CV results (Figure 4a).

The effect of Hc contents on Li–S battery performances was evaluated, and the results show that the battery performance is optimal when the mass ratio of Hc was 1.5% in the cathode (Figure S19). Rate capacities of CNTs-S/DHcs, CNTs-S/Hcs, and CNTs-S cathodes were evaluated at different current densities. As shown in Figure 4c, it is obvious that, with the addition of Hc, the cathodes demonstrate enhanced capacities at all measured current densities. Especially, when DHcs is introduced, battery capacities of 1472.1, 996.6, 898.6, 858.5, and 817.0 mAh g<sup>-1</sup> are achieved at 0.2, 0.5, 0.8, 1.0, and 1.5 C, respectively, which are superior to those of its counterparts and

most of the other reported protein materials (Figure S20).<sup>21,33–39</sup> When the current density is abruptly reduced back to 0.2 C, the capacity of CNTs-S/DHcs cathode remains close to that of the previous cycles at the same rate, illustrating the excellent reaction reversibility.

In terms of the cycling properties at 0.5 C with a low sulfur loading in Figure 4d, the CNTs-S/DHcs cathode has a more stable curve and a discharge capacity of 751.0 mAh g<sup>-1</sup> after 160 cycles, corresponding to a high capacity retention rate of 71.2% and a low capacity decay rate of 0.18% per cycle. Meantime, the Coulombic efficiency for the CNTs-S/DHcs cathode is close to ~100% through all long-cycle tests. However, the control cathodes without DHcs (CNTs-S/Hcs and CNTs-S) only deliver initial discharge capacities of 923.2 (CNTs-S/Hcs) and 801.4 mAh g<sup>-1</sup> (CNTs-S) and the capacity decay rates are 0.20% (CNTs-S/Hcs) and 0.30% (CNTs-S), respectively. The capacity retention of the CNTs-S/DHcs cathode is still impressive as the rate increases to 1.0 C, with 860.7 mAh g<sup>-1</sup> of its first capacity, a capacity decay rate of 0.08% per cycle, and 98.9% Coulombic efficiency after 360 cycles (Figure 4e).

The good rate capability, reversability, and cyclability of CNTs-S/DHcs can be ascribed to the highly catalytic DHcs with more exposure of Cu, O, and N active sites, smaller steric hindrance, and high gelation, which can strongly chemisorb/catalyze sulfur species at the microenvironment, boost the fast electron/ion transport, and strengthen the contact at the electrode/electrolyte interface, leading to a reduced loss of active materials and smooth sulfur conversion kinetics in the working batteries. The favorable interfacial reaction kinetics on the CNTs-S/DHcs electrode was also confirmed by an electrochemical impedance spectroscopy (EIS) analysis detailed in Figure S21 and Table S1, in which the  $R_{ct}$  value presents the descending order CNTs-S > CNTs-S/Hcs > CNTs-S/DHcs, indicating the beneficial enhancement of electron/ion conductivity due to DHcs.<sup>40</sup> In this case, even under the high sulfur loading (4.3 mg cm<sup>-2</sup>) and poor electrolyte/sulfur (E/S) ratio (8 μL mg<sup>-1</sup>) conditions shown in Figure 4f, the CNTs-S/DHcs-based batteries still demonstrate considerable initial capacities of 1014.5 mAh g<sup>-1</sup> at 0.1 C, as well as a high capacity retention of 70.3% and areal capacity of 3.07 mAh cm<sup>-2</sup> after 100 cycles, which are higher than those observed for the other two batteries.

*In situ* methods without disassembly of a battery, including *in situ* UV–vis spectroscopy, *in situ* Raman spectroscopy, and quasi *in situ* XPS spectroscopy, were employed to monitor the reaction pathways in real time in Li–S batteries. The absorption spectra for CNTs-DHcs, CNTs-Hcs, and CNTs cathodes during the discharging process are revealed in Figure S22. According to different intermediates' peak positions ( $S_8^{2-}$  at 492 nm,  $S_4^{2-}$  at 435 nm,  $S_3^{*-}$  at 617 nm),<sup>41</sup> the UV–vis spectral intensities of the sulfur species at different electrode surfaces were extracted and analyzed as the potential was negatively scanned (Figure S23). On discharging from 2.8 to 1.6 V, the  $S_8^{2-}$  and  $S_4^{2-}$  peak intensities gradually decrease, while the  $S_3^{*-}$  peak intensity increases at the three cathodes, which are attributed to the reaction from long-chain LiPSs to short-chain LiPSs. It is of interest that CNTs-DHcs has the fastest intensity changes of the sulfur species among the three electrodes, implying that DHcs can more effectively catalyze LiPSs to form Li<sub>2</sub>S due to the polar Cu, O, and N sites in DHcs. This finding is in agreement with the *in situ* Raman and quasi *in situ* XPS analysis. Figure 5a–c and Figure S24 give the

Raman spectra and the corresponding contour profiles collected on the three cathodes during the discharge process. Five characteristic peaks for  $S_8$  (152, 246, 437, and 472 cm<sup>-1</sup>) and  $S_8^{2-}$  (219 cm<sup>-1</sup>)<sup>42,43</sup> are detected in all cathodes at 2.8 V. When the cathode is discharged to 2.3 V, the above five peaks largely fade and one new peak at 120 cm<sup>-1</sup> due to  $S_5^{2-}$  species<sup>44,45</sup> appears on the CNTs-S/DHcs cathode. This manifests that  $S_8$  is transformed to long-chain LiPSs. On further discharging to 1.6 V, the  $S_8$ ,  $S_8^{2-}$ , and  $S_5^{2-}$  peaks disappear completely and the peak of Li<sub>2</sub>S<sub>2</sub> is detected from the CNTs-S/DHcs cathode, which showed the further transformation of long-chain LiPSs to solid Li<sub>2</sub>S<sub>2</sub>/Li<sub>2</sub>S. A similar robust sulfur conversion process is also observed in the S 2p (Figure 5d) and Li 1s (Figure S25) XPS spectra of the CNTs-S/DHcs cathode, where  $S_8$  is first transformed to Li<sub>2</sub>S<sub>n</sub> (8 ≥ n ≥ 4) and partial Li<sub>2</sub>S<sub>2</sub>/Li<sub>2</sub>S at 2.1 V and then to large amounts of Li<sub>2</sub>S<sub>2</sub>/Li<sub>2</sub>S, accompanied by a large shift of the Li–S bond to lower binding energy, indicating that LiPSs gain more electrons from DHcs and are reduced during discharge. In comparison, this polysulfide transformation is almost ineffective on the other two cathodes, particularly on the CNTs-S cathode, as demonstrated by both *in situ* Raman (Figure 5b,c and Figure S24b,c) and quasi *in situ* S 2p and Li 1s XPS results (Figure 5e,f), confirming the unique mechanism of DHcs in SRR again. All of the quasi *in situ* findings demonstrate that the reaction mechanism of the CNTs-S/DHcs cell is based on the formation of  $S_5^{2-}$  and  $S_3^{*-}$  intermediates, which is distinguished from the traditional SRR pathway (i.e.,  $S_8^{2-} \rightarrow S_6^{2-} \rightarrow S_4^{2-} \rightarrow S_2^{2-} \rightarrow S^{2-}$ )<sup>46</sup> and further shows the excellent catalytic function of DHcs.

### 3. CONCLUSIONS

In summary, we have designed and fabricated a novel polysulfide catalyst derived from DHc to address the shuttle effect and sluggish sulfur conversion kinetics issues in Li–S batteries. Benefiting from the unfolded architecture of the reformed natural enzyme, reduced steric hindrance for the entry of LiPSs, increased channels for electron/ion transport into the center Cu core, and sufficient O- and N-containing functional groups exposed on its side chains, as well as the transformation of intermolecular H-bonds, the DHcs present great effectiveness in improving the mechanical durability of the electrode and adsorbing and transforming LiPSs, as well as facilitating Li<sup>+</sup> transport, which lower the activation energy barrier from LiPSs to solid Li<sub>2</sub>S/Li<sub>2</sub>S<sub>2</sub> and effectively enhance the redox kinetics of LiPSs. As a result, the DHc greatly improves Li–S battery performances in rate capacity and cycle stability. This work provides a new perspective and an experimental basis for developing reformed natural enzymes as catalyst materials for high-performance Li–S batteries.

### ■ ASSOCIATED CONTENT

#### Supporting Information

The Supporting Information is available free of charge at <https://pubs.acs.org/doi/10.1021/acsami.2c18976>.

Experimental details and additional figures, including XRD patterns, digital photos, SEM images, XPS spectra, electrochemical performance and corresponding analysis, comparison between CNTs/S-DHcs electrode and others protein-based systems, *in situ* UV–vis absorption and related analysis, *in situ* Raman spectra, and quasi *in situ* XPS spectra (PDF)

## AUTHOR INFORMATION

## Corresponding Authors

**Shuo Yang** – Key Laboratory of Carbon Materials of Zhejiang Province and College of Electrical and Electronic Engineering, Wenzhou University, Wenzhou 325035, People's Republic of China; [orcid.org/0000-0001-8906-5289](https://orcid.org/0000-0001-8906-5289);

Email: [yangshuo@wzu.edu.cn](mailto:yangshuo@wzu.edu.cn)

**Dong Cai** – Key Laboratory of Carbon Materials of Zhejiang Province, Wenzhou University, Wenzhou 325035, People's Republic of China; Email: [caidong@wzu.edu.cn](mailto:caidong@wzu.edu.cn)

**Huagui Nie** – Key Laboratory of Carbon Materials of Zhejiang Province, Wenzhou University, Wenzhou 325035, People's Republic of China; Email: [huaguinie@126.com](mailto:huaguinie@126.com)

**Zhi Yang** – Key Laboratory of Carbon Materials of Zhejiang Province, Wenzhou University, Wenzhou 325035, People's Republic of China; [orcid.org/0000-0002-9265-5041](https://orcid.org/0000-0002-9265-5041);

Email: [yang201079@126.com](mailto:yang201079@126.com)

## Authors

**Ce Liang** – Key Laboratory of Carbon Materials of Zhejiang Province, Wenzhou University, Wenzhou 325035, People's Republic of China

**Jun Liu** – Guangdong Provincial Key Laboratory of Advanced Energy Storage Materials, School of Materials Science and Engineering, South China University of Technology, Guangzhou 510641, People's Republic of China;

[orcid.org/0000-0002-7078-8046](https://orcid.org/0000-0002-7078-8046)

**Shuang Yu** – Key Laboratory of Carbon Materials of Zhejiang Province, Wenzhou University, Wenzhou 325035, People's Republic of China

**Tingting Li** – Key Laboratory of Carbon Materials of Zhejiang Province, Wenzhou University, Wenzhou 325035, People's Republic of China

**Haohao Wang** – College of Electrical and Electronic Engineering, Wenzhou University, Wenzhou 325035, People's Republic of China

**Yahui Liu** – Key Laboratory of Carbon Materials of Zhejiang Province, Wenzhou University, Wenzhou 325035, People's Republic of China

Complete contact information is available at:

<https://pubs.acs.org/10.1021/acsami.2c18976>

## Author Contributions

C.L., S.Y., T.L., and H.N. performed all the experiments. J.L., H.W., and Y.L. analyzed the data and prepared the results. S.Y., D.C., and H.N. planned the study and composed the manuscript. Z.Y. conceived and supervised the project.

## Notes

The authors declare no competing financial interest.

## ACKNOWLEDGMENTS

This research was funded in part by the National Natural Science Foundation of China (Grant Nos. 22109119, 21875166, and U21A2081), the Natural Science Foundation of Zhejiang Province (Grant No. LQ22B030003), the Major Scientific and Technological Innovation Project of Wenzhou City (Grant No. ZG2021013), and the Open Fund of Guangdong Provincial Key Laboratory of Advanced Energy Storage Materials, South China University of Technology (Grant No. AESM202104).

## REFERENCES

- (1) Zhao, M.; Li, X.-Y.; Chen, X.; Li, B.-Q.; Kaskel, S.; Zhang, Q.; Huang, J.-Q. Promoting the Sulfur Redox Kinetics by Mixed Organodiselenides in High-Energy-Density Lithium–Sulfur Batteries. *eScience* **2021**, *1* (1), 44–52.
- (2) Yue, X.-Y.; Zhang, J.; Bao, J.; Bai, Y.-F.; Li, X.-L.; Yang, S.-Y.; Fu, Z.-W.; Wang, Z.-H.; Zhou, Y.-N. Sputtered MoN Nanolayer as a Multifunctional Polysulfide Catalyst for High-Performance Lithium–Sulfur Batteries. *eScience* **2022**, *2* (3), 329–338.
- (3) Zhao, M.; Peng, Y.-Q.; Li, B.-Q.; Zhang, X.-Q.; Huang, J.-Q. Regulation of Carbon Distribution to Construct High-Sulfur-Content Cathode in Lithium–Sulfur Batteries. *J. Energy Chem.* **2021**, *56*, 203–208.
- (4) Chen, Z. X.; Zhao, M.; Hou, L. P.; Zhang, X. Q.; Li, B. Q.; Huang, J. Q. Toward Practical High-Energy-Density Lithium–Sulfur Pouch Cells: A Review. *Adv. Mater.* **2022**, *34* (35), 2201555.
- (5) Bi, C. X.; Zhao, M.; Hou, L. P.; Chen, Z. X.; Zhang, X. Q.; Li, B. Q.; Yuan, H.; Huang, J. Q. Anode Material Options Toward 500 Wh kg<sup>-1</sup> Lithium–Sulfur Batteries. *Adv. Sci.* **2022**, *9* (2), 2103910.
- (6) Du, Z.; Chen, X.; Hu, W.; Chuang, C.; Xie, S.; Hu, A.; Yan, W.; Kong, X.; Wu, X.; Ji, H.; Wan, L. J. Cobalt in Nitrogen-Doped Graphene as Single-Atom Catalyst for High-Sulfur Content Lithium–Sulfur Batteries. *J. Am. Chem. Soc.* **2019**, *141* (9), 3977–3985.
- (7) Ma, F.; Wan, Y.; Wang, X.; Wang, X.; Liang, J.; Miao, Z.; Wang, T.; Ma, C.; Lu, G.; Han, J.; Huang, Y.; Li, Q. Bifunctional Atomically Dispersed Mo–N<sub>2</sub>/C Nanosheets Boost Lithium Sulfide Deposition/Decomposition for Stable Lithium–Sulfur Batteries. *ACS Nano* **2020**, *14* (8), 10115–10126.
- (8) Li, Q.; Ma, Z.; Zhao, J.; Shen, K.; Shi, T.; Xie, Y.; Fan, Y.; Qin, X.; Shao, G. A Flexible Self-Supporting Ultralong MnO<sub>2</sub> Nanowires-Expanded Graphite Nanosheets Current Collector with Enhanced Catalytic Reaction Kinetics for High-Loading Lithium–Sulfur Batteries. *J. Power Sources* **2022**, *521*, 230929.
- (9) Gao, X.-T.; Xie, Y.; Zhu, X.-D.; Sun, K.-N.; Xie, X.-M.; Liu, Y.-T.; Yu, J.-Y.; Ding, B. Li–S Batteries: Ultrathin MXene Nanosheets Decorated with TiO<sub>2</sub> Quantum Dots as an Efficient Sulfur Host toward Fast and Stable Li–S Batteries. *Small* **2018**, *14* (41), 1870190.
- (10) Wei, C.; Tian, M.; Wang, M.; Shi, Z.; Yu, L.; Li, S.; Fan, Z.; Yang, R.; Sun, J. Universal in Situ Crafted MO<sub>x</sub>-MXene Heterostructures as Heavy and Multifunctional Hosts for 3D-Printed Li–S Batteries. *ACS Nano* **2020**, *14* (11), 16073–16084.
- (11) Yang, L.; Manithody, C.; Rezaie, A. R. Activation of Protein C by the Thrombin-Thrombomodulin Complex: Cooperative Roles of Arg-35 of Thrombin and Arg-67 of Protein C. *Proc. Natl. Acad. Sci. U. S. A.* **2006**, *103* (4), 879–884.
- (12) Harris, J. R.; Markl, J. Keyhole Limpet Hemocyanin: Molecular Structure of a Potent Marine Immunoactivator. *Eur. Urol.* **2000**, *37* (3), 24–33.
- (13) Dong, Y.; Cai, D.; Li, T.; Yang, S.; Zhou, X.; Ge, Y.; Tang, H.; Nie, H.; Yang, Z. Sulfur Reduction Catalyst Design Inspired by Elemental Periodic Expansion Concept for Lithium–Sulfur Batteries. *ACS Nano* **2022**, *16* (4), 6414–6425.
- (14) Otten, R.; Liu, L.; Kenner, L. R.; Clarkon, M. W.; Mavor, D.; Tawfik, D. S.; Kern, D.; Fraser, J. S. Rescue of Conformational Dynamics in Enzyme Catalysis by Directed Evolution. *Nat. Commun.* **2018**, *9*, 1314.
- (15) Markel, U.; Essani, K. D.; Besirlioglu, V.; Schiffels, J.; Streit, W. R.; Schwaneberg, U. Advances in Ultrahigh-Throughput Screening for Directed Enzyme Evolution. *Chem. Soc. Rev.* **2020**, *49* (1), 233–262.
- (16) Gatsogiannis, C.; Markl, J. Keyhole Limpet Hemocyanin: 9-Å CryoEM Structure and Molecular Model of the KLH1 Dodecamer Reveal the Interfaces and Intricate Topology of the 160 Functional Units. *J. Mol. Biol.* **2009**, *385* (3), 963–983.
- (17) Fan, Y.; Zeng, G.; Liu, J.; Chen, H.; Xue, J.; Wu, Y.; Li, X. Spectroscopic Studies on the Interaction of Chromium (VI) and Chromium (III) with Keyhole Limpet Hemocyanin. *Luminescence* **2017**, *32* (2), 190–194.

- (18) Yamada, K.; Tsuboi, Y.; Itaya, A. AFM Observation of Silk Fibroin on Mica Substrates: Morphologies Reflecting the Secondary Structures. *Thin Solid Films* **2003**, *440* (1–2), 208–216.
- (19) Wang, T.; Li, Y.; Zhang, J.; Yan, K.; Jaumaux, P.; Yang, J.; Wang, C.; Shanmukaraj, D.; Sun, B.; Armand, M.; Cui, Y.; Wang, G. Immunizing Lithium Metal Anodes Against Dendrite Growth Using Protein Molecules to Achieve High Energy Batteries. *Nat. Commun.* **2020**, *11*, 5429.
- (20) Li, X.; Yuan, L.; Liu, D.; Liao, M.; Chen, J.; Yuan, K.; Xiang, J.; Li, Z.; Huang, Y. Elevated Lithium Ion Regulation by a “Natural Silk” Modified Separator for High-Performance Lithium Metal Anode. *Adv. Funct. Mater.* **2021**, *31* (18), 2100537.
- (21) Chen, M.; Li, C.; Fu, X.; Wei, W.; Fan, X.; Hattori, A.; Chen, Z.; Liu, J.; Zhong, W. H. Let It Catch: A Short-Branched Protein for Efficiently Capturing Polysulfides in Lithium–Sulfur Batteries. *Adv. Energy Mater.* **2020**, *10* (9), 1903642.
- (22) Zakharova, I. A.; Salyn, J. V.; Tatjanenko, L. V.; Mashkovsky, Y. S.; Ponticelli, G. Inhibitory Activity of Palladium(II) and Platinum(II) Complexes with Isoxazole and Its Derivatives. *J. Inorg. Biochem.* **1981**, *15* (1), 89–92.
- (23) Anson, M. L.; Mirsky, A. E. The Effect of Denaturation on the Viscosity of Protein Systems. *J. Gen. Physiol.* **1932**, *15* (3), 341–350.
- (24) Li, J.; Qu, Y.; Chen, C.; Zhang, X.; Shao, M. Theoretical Investigation on Lithium Polysulfide Adsorption and Conversion for High-Performance Li–S Batteries. *Nanoscale* **2021**, *13* (1), 15–35.
- (25) Reuter, F. S.; Huang, C. J.; Hsieh, Y. C.; Dörfler, S.; Brunklaus, G.; Althues, H.; Winter, M.; Lin, S. D.; Hwang, B. J.; Kaskel, S. Stabilizing Effect of Polysulfides on Lithium Metal Anodes in Sparingly Solvating Solvents. *Batteries Supercaps.* **2021**, *4* (2), 347–358.
- (26) Hou, L. P.; Li, Z.; Yao, N.; Bi, C. X.; Li, B. Q.; Chen, X.; Zhang, X. Q.; Zhang, Q. Weakening the Solvating Power of Solvents to Encapsulate Lithium Polysulfides Enables Long-Cycling Lithium–Sulfur Batteries. *Adv. Mater.* **2022**, *34* (45), 2205284.
- (27) Hou, T. Z.; Xu, W. T.; Chen, X.; Peng, H. J.; Huang, J. Q.; Zhang, Q. Lithium Bond Chemistry in Lithium–Sulfur Batteries. *Angew. Chem., Int. Ed.* **2017**, *56* (28), 8178–8182.
- (28) Peng, H. J.; Zhang, Z. W.; Huang, J. Q.; Zhang, G.; Xie, J.; Xu, W. T.; Shi, J. L.; Chen, X.; Cheng, X. B.; Zhang, Q. A Cooperative Interface for Highly Efficient Lithium–Sulfur Batteries. *Adv. Mater.* **2016**, *28* (43), 9551–9558.
- (29) Han, F.; Yue, J.; Fan, X.; Gao, T.; Luo, C.; Ma, Z.; Suo, L.; Wang, C. High-Performance All-Solid-State Lithium–Sulfur Battery Enabled by a Mixed-Conductive  $\text{Li}_2\text{S}$  Nanocomposite. *Nano Lett.* **2016**, *16* (7), 4521–4527.
- (30) Wang, Z.; Ji, H.; Zhou, L.; Shen, X.; Gao, L.; Liu, J.; Yang, T.; Qian, T.; Yan, C. All-Liquid-Phase Reaction Mechanism Enabling Cryogenic Li–S Batteries. *ACS Nano* **2021**, *15* (8), 13847–13856.
- (31) Wang, M.; Fan, L.; Qiu, Y.; Chen, D.; Wu, X.; Zhao, C.; Cheng, J.; Wang, Y.; Zhang, N.; Sun, K. Electrochemically Active Separators with Excellent Catalytic Ability toward High-Performance Li–S Batteries. *J. Mater. Chem. A* **2018**, *6* (25), 11694–11699.
- (32) Liang, L.; Niu, L.; Wu, T.; Zhou, D.; Xiao, Z. Fluorine-Free Fabrication of MXene via Photo-Fenton Approach for Advanced Lithium–Sulfur Batteries. *ACS Nano* **2022**, *16* (5), 7971–7981.
- (33) Fu, X.; Li, C.; Wang, Y.; Scudiero, L.; Liu, J.; Zhong, W. H. Self-Assembled Protein Nanofilter for Trapping Polysulfides and Promoting  $\text{Li}^+$  Transport in Lithium–Sulfur Batteries. *J. Phys. Chem. Lett.* **2018**, *9* (10), 2450–2459.
- (34) Wu, H.; Wu, Q.; Chu, F.; Hu, J.; Cui, Y.; Yin, C.; Li, C. Sericin Protein as a Conformal Protective Layer to Enable Air-Endurable Li Metal Anodes and High-Rate Li–S Batteries. *J. Power Sources* **2019**, *419*, 72–81.
- (35) Wang, H.; Wang, Y.; Zheng, P.; Yang, Y.; Chen, Y.; Cao, Y.; Deng, Y.; Wang, C. Self-Healing Double-Cross-Linked Supramolecular Binders of a Polyacrylamide-Grafted Soy Protein Isolate for Li–S Batteries. *ACS Sustain. Chem. Eng.* **2020**, *8* (34), 12799–12808.
- (36) Chen, M.; Fu, X.; Liu, J.; Chen, Z.; Zhong, W. H. A Protein-Based Janus Separator for Trapping Polysulfides and Regulating Ion Transport in Lithium–Sulfur Batteries. *ChemSusChem* **2021**, *14* (10), 2226–2236.
- (37) Wang, H.; Wang, Y.; Zhang, G.; Yang, Z.; Chen, Y.; Deng, Y.; Yang, Y.; Wang, C. Water-Based Dual-Network Conductive Polymer Binders for High-Performance Li–S Batteries. *Electrochim. Acta* **2021**, *371*, 137822.
- (38) Qiu, J.; Wu, S.; Yang, Y.; Xiao, H.; Wei, X.; Zhang, B.; Hui, K. N.; Lin, Z. Aqueous Supramolecular Binder for a Lithium–Sulfur Battery with Flame-Retardant Property. *ACS Appl. Mater. Interfaces* **2021**, *13* (46), 55092–55101.
- (39) Wang, H.; Yang, Y.; Zheng, P.; Wang, Y.; Ng, S.-W.; Chen, Y.; Deng, Y.; Zheng, Z.; Wang, C. Water-Based Phytic Acid-Crosslinked Supramolecular Binders for Lithium–Sulfur Batteries. *Chem. Eng. J.* **2020**, *395*, 124981.
- (40) Li, Y.; Lei, X.; Yuan, Y.; Wu, S.; Han, B.; Liu, X.; Liu, W.; Hu, J.; Yang, C.; Lin, Z.; Lu, J.  $\text{Fe}_3\text{P}$ -Decorated N,P Codoped Carbon Synthesized via Direct Biological Recycling for Endurable Sulfur Encapsulation. *ACS Cent. Sci.* **2020**, *6* (10), 1827–1834.
- (41) Zhou, S.; Yang, S.; Ding, X.; Lai, Y.; Nie, H.; Zhang, Y.; Chan, D.; Duan, H.; Huang, S.; Yang, Z. Dual-Regulation Strategy to Improve Anchoring and Conversion of Polysulfides in Lithium–Sulfur Batteries. *ACS Nano* **2020**, *14* (6), 7538–7551.
- (42) Zhou, S.; Yang, S.; Cai, D.; Liang, C.; Yu, S.; Hu, Y.; Nie, H.; Yang, Z. Cofactor-Assisted Artificial Enzyme with Multiple Li-Bond Networks for Sustainable Polysulfide Conversion in Lithium–Sulfur Batteries. *Adv. Sci.* **2022**, *9* (3), 2104205.
- (43) Zhang, Y.; Yang, S.; Zhou, S.; Zhang, L.; Gu, B.; Dong, Y.; Kong, S.; Cai, D.; Fang, G.; Nie, H.; Yang, Z. Oxygen Doping in Antimony Sulfide Nanosheets to Facilitate Catalytic Conversion of Polysulfides for Lithium–Sulfur Batteries. *Chem. Commun.* **2021**, *57* (26), 3255–3258.
- (44) Xue, L.; Li, Y.; Hu, A.; Zhou, M.; Chen, W.; Lei, T.; Yan, Y.; Huang, J.; Yang, C.; Wang, X.; Hu, Y.; Xiong, J. In Situ/Operando Raman Techniques in Lithium–Sulfur Batteries. *Small Struct.* **2022**, *3*, 2100170.
- (45) Xu, R.; Tang, H.; Zhou, Y.; Wang, F.; Wang, H.; Shao, M.; Li, C.; Wei, Z. Enhanced Catalysis of Radical-To-Polysulfide Interconversion via Increased Sulfur Vacancies in Lithium–Sulfur Batteries. *Chem. Sci.* **2022**, *13* (21), 6224–6232.
- (46) Hua, W.; Yang, Z.; Nie, H.; Li, Z.; Yang, J.; Guo, Z.; Ruan, C.; Chen, X.; Huang, S. Polysulfide-Scission Reagents for the Suppression of the Shuttle Effect in Lithium–Sulfur Batteries. *ACS Nano* **2017**, *11* (2), 2209–2218.